Reversible Light-Triggered Stretching of Small-Molecule Photochromic Organic Nanoparticles

Etienne Bequet-Ermoy, Virginie Silvestre, Stéphane Cuenot, Eléna Ishow

RESEARCH ARTICLE

NANO · MICRO small
www.small-journal.com

Reversible Light-Triggered Stretching of Small-Molecule Photochromic Organic Nanoparticles

Etienne Bequet-Ermoy, Virginie Silvestre, Stéphane Cuenot, and Eléna Ishow**

Functional organic nanomaterials are nowadays largely spread in the field of nanomedicine. In situ modulation of their morphology is thus expected to considerably impact their interactions with the surroundings. In this context, photoswitchable nanoparticles that are manufactured, amenable to extensive disassembling upon illumination in the visible, and reversible reshaping under UV exposure. Such reversibility turns to be strongly impaired for photochromic nanoparticles in close contact with a substrate. In situ atomic force microscopy investigations at the nanoscale actually reveal progressive disintegration of the organic nanoparticles under successive UV–vis cycles of irradiation, in the absence of intrinsic elastic forces. These results point out the dramatic interactions exerted by surfaces on the cohesion of non-covalently bonded organic nanoparticles. They invite to harness such systems, often used as biomarkers, to also serve as photoactivatable drug delivery nanocarriers.

1. Introduction

Triggering the geometry of photoresponsive organic materials using light activation[1] represents a fascinating approach for the remote controls of surface hydrophilicity[2] and wettability,[3] cell adhesion,[4] or optical waveguides[5] to cite only a few. Reversibility is smartly accomplished by incorporating photochromic dyes characterized by efficient photoconversion between two stable states, each addressable at a specific wavelength from the Ultraviolet (UV) to the near- infrared range[6–8] while striving to reduce the delivered energy.[9] In order to improve the efficacy of shape modulation in the solid state, molecular ordering, promoting tight intermolecular interactions and cooperativity, is highly beneficial.[10,11] The first strategy hinges on liquid crystalline polymers,[12,13] incorporating photochromes in the main chain, and producing impressive macroscopic bending,[14] twisting[15] or oscillation[16] from microscopic synergy under isotropic or polarized illumination.[17] The second strategy relies on molecular crystals where collective response of the interacting photochromes revisited the mechanical properties of organic crystals.[18] Two seminal works demonstrated remarkable elastic UV-induced deformation of micrometer-thin crystals made of anthracenyl units[19] or dithienylethenes,[20] the latter displaying full reversibility after exposure to visible light. More recently, light-controlled phase transitions of crystals into a gel, glassy, or liquid state[21] have stirred particular attraction for their potential to restitute stored energy as solar thermal fuels,[22] or convert the phase change into mechanical works, by opening the road toward nanorobots[23] and photoremovable adhesives.[24] Finally, a third family of photoactive materials, made exclusively out of small molecules substituted with bulky groups, and displaying amorphous glassy properties, showed stunning macroscopic deformation when monomeric azo thin films[25,26] were subjected to interferential polarized illumination, due to collective dye migration in an external optical gradient field.[27] The amplitude and rate of the deformation were found to be directly governed by the steric and electronic interactions between the azo substituents.[28,29] Nowadays, going down the scale until reaching nanoparticle dimensions, while keeping tight cohesion, can easily be achieved by resorting to nanoprecipitation of small hydrophobic dyes in water.[30–32] Confinement effects, mainly promoted by $\pi-\pi$ stacking of the aromatic backbones, leads to considerably amplified and ultrafast energy and electron transfers due to the close vicinity of the photoactive dyes.[33–35] Hence, nonlinear fluorescence quenching could be observed in composite nanoparticles made out of self-assembled fluorophores and diarylethenes[36,37] or azo[38] photochromes acting as energy or electron traps respectively. Exploiting this spatial vicinity to induce cooperative geometrical changes in small molecule-based nanoparticles has however been scarcely harnessed. Photochromic microspheres constituted of self-assembled amphiphilic diarylethenes showed the formation of

E. Bequet-Ermoy, V. Silvestre, E. Ishow
Nantes Université, CNRS
CEISAM
UMR 6230, Nantes F-44000, France
E-mail: elena.ishow@univ-nantes.fr
S. Cuenot
Institut des Matériaux de Nantes Jean Rouxel
CNRS
Nantes Université
IMN, Nantes F-44000, France
E-mail: stephane.cuenot@cnrs-imn.fr

The ORCID identification number(s) for the author(s) of this article can be found under https://doi.org/10.1002/smll.202403912

DOI: 10.1002/smll.202403912

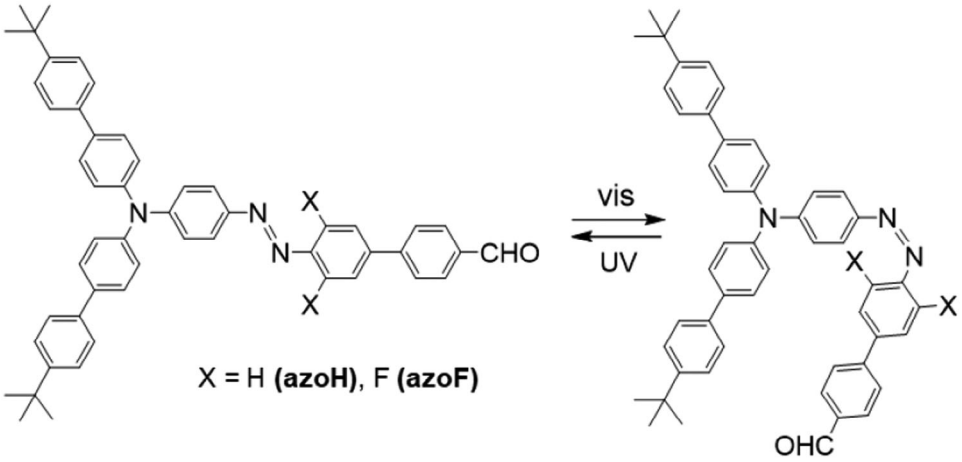

Scheme 1. Structure and *E*-*Z* photoisomerization reactions of **azoH** and **azoF**.

nanometer filaments at their surface upon UV irradiation as a result of phase transition.[39] Nevertheless, the morphological transformation is quite limited due to the small structural changes undergone between the open and planarized closed forms. Conversely, azo compounds, endowed with subsequent contraction/elongation of the azo *E* and *Z* photoisomers after UV and vis irradiations respectively, impart self-assemblies with remarkable transformation capability. A first work with azo photochromes, comprising the 4-biphenylcarbonitrile mesogenic unit, described the reversible generation of microspheres from an homogeneous aqueous solution under UV illumination.[40] Later on, azo self-assemblies, based on 1,3,5-benzene tricarboxamide discotic units and forming micro- and nanofibers in their initial *E*-state in water, underwent by contrast full dissolution upon UV illumination.[41,42] Following the abovementioned examples, symmetrical or weakly polar azo derivatives have so far mostly been considered since switching between their *E* and *Z* isomers can be performed by exciting their energy-distinct $\pi\pi^*$ and $n\pi^*$ transitions. However, as noticed, the increase in dipole moment occurring upon *E*-to-*Z* photoisomerization causes severe changes in the mutual interactions between the azo self-assemblies and their aqueous surroundings. The irreversible collapse of azo-coated metallic nanoparticles into larger aggregates progressively occurs in the absence of surfactant.[43] The incorporation of polar and hydrophilic ligands into the azo shell contributed to stabilize the aqueous nanoparticle dispersions thanks to favorable dipole-dipole interactions with the water solvation.[44] Nevertheless, back thermal relaxation of the UV-photogenerated *Z* isomers was considerably accelerated by up to three orders of magnitude.[45] Hence, ensuring colloidal stability while maintaining thermal stability of the photoinduced changes becomes a major challenge for aqueous dispersions of neutral organic nanoparticles.

To solve this dilemma, we want herein to demonstrate that both colloidal stability and reversible photoswitching of azo nanoparticles in water can eventually be achieved with pseudo-stilbene azo compounds, incorporating *o*-fluorinated phenyl units, known to bring large thermal stability of the *Z* isomers.[46,47] To this aim, we have retained azo compounds, allowing for dual-wavelength excitation and yielding large modulations of the nanoparticle geometry, that have been addressed at the nanoscale by combining atomic force microscopy and in situ irradiation. Such delicate measurements importantly question the experimental conditions adopted to investigate the photomechanical response of photochromic nanoparticle dispersions as a function of their close environment.

2. Results and Discussion

2.1. Azo Engineering and Impact of Ortho-Fluorine Substitution

Following previous works on photoactive nanoparticles and azo polar compounds,[38,48] we have retained a bulky and twisted electron-donating triphenylamino group, creating enough disorder and free volume to yield an amorphous phase, and thus permit photoisomerization in the hydrated solid state, as described in **Scheme 1**.[49]

In order to endow the azo unit with strong charge transfer, an additional electron-withdrawing carbonyl group has been introduced along the main azo bond direction (Scheme S1; Figures S1–S12, Supporting Information). Substitution with fluorine atoms was performed on the side of the electron-poor carbonyl substituent to reinforce charge transfer and yield compound **azoF**. Interestingly, the expected glassy properties, characterized by differential scanning calorimetry, were identified at lower temperature for **azoF**, with values of glass transition temperature T_g found at 100 °C against 119 °C for **azoH** (Figure S13, Supporting Information). This discrepancy is likely to stem from the more distorted **azoF** backbone (dihedral angle of 31° between the azo phenyl rings), preventing extensive intermolecular interactions upon $\pi-\pi$ aggregation in the solid state, as established from geometry optimization using quantum computations (Figures S14 and S15, Supporting Information). The slight but significant differences between both compounds were also noted in the absorption spectra (**Figure 1a**). While the absorption maximum in tetrahydrofuran (THF) solution underwent an 8 nm bathochromic shift from 464 nm for **azoH** to 472 nm for the similar fluorinated azo derivative **azoF**, the second band in

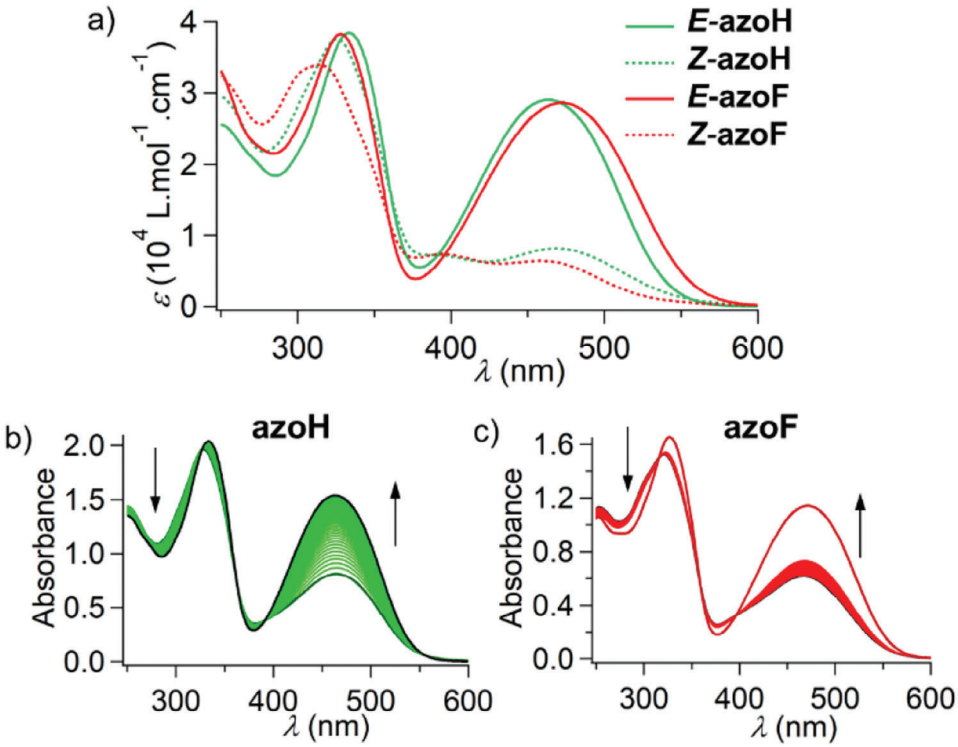

Figure 1. Absorption spectra of **azoH** and **azoF** in THF solution. a) *E* and *Z* isomers, the latter being inferred from Fisher's method for **azoH** and ^{1}H NMR measurements for **azoF**. b) Back thermal relaxation in the dark from the **azoH** photostationary state reached after irradiation at 550 nm (total recording time: 16 h). c) Back thermal relaxation in the dark from the **azoF** photostationary state reached after irradiation at 550 nm (total recording time: 24 h to vary from 0.63 to 0.73); the upper curve corresponds to that of the *E* isomer before irradiation).

the UV range displayed a hypsochromic shift from 333 nm for **azoH** to 327 nm for **azoF** (**Table 1**; Figure 1a).

From time-dependent density functional theory (TD-DFT), the latter band results from overlapping transitions, involving charge transfer from the central nitrogen to the peripheral biphenyl arms as well as $\pi\pi^*$ transitions centered on the azo central region (Figures S14 and S15, Supporting Information). When going from THF solution to nanoparticle dispersion in water, the maximum absorption wavelengths were found 10 nm longer, as a result of the increase in polarity exerted by each azo dye

Table 1. Photophysical and photochromic properties of **azoH** and **azoF** in THF solution.

Cpd	λ_{max} [nm] (ϵ_{max} [10^4 L.mol^{-1}.cm^{-1}])		$\rho_{E\to Z}$ [%][a] (λ_{irr} 550 nm) (λ_{irr} 488 nm)	$\rho_{Z\to E}$ [%][b] (λ_{irr} 365 nm)	τ (Z) [h][c]
	E-isomer	Z-isomer			
azoH	464 (2.90)	468 (0.81)	62	65	2.5
	333 (3.84)	325 (3.76)	81		
azoF	472 (2.86)	460 (0.64)	65	63	57
	327 (3.83)	317 (3.39)	63		

[a] Determined from Fisher's method for **azoH** and ^{1}H NMR spectra for **azoF**; [b] Inferred from the absorption spectra for the (*Z*)-isomer calculated after irradiation in the visible range; [c] Back thermal relaxation at 20 °C of a solution irradiated at 550 nm at the photostationary state, modeled by a first-order kinetics.

whose dipole moment was calculated to be 7.40 and 6.46 Debye for ***E*-azoH** and ***E*-azoF** respectively in THF solution. In order to assess the photochromic potentiality of both **azoH** and **azoF** dyes, irradiation was first performed in THF solution at 488 nm, close to the absorption maximum wavelength. A neat decrease of the absorption band in the visible could be observed while isosbestic points at 397 and 392 nm featured the *E*-*Z* equilibrium for **azoH** and **azoF**, respectively (Figure 1b). Contrary to the very similar changes in absorption, the back thermal relaxation dramatically differs between **azoH** and **azoF**. The rate constant k_{ZE} was indeed found to be 4.88×10^{-6} s^{-1} (time constant τ(Z) ≈57 h) for **azoF** against 1.09×10^{-4} s^{-1} (time τ(Z) ≈2.5 h) for **azoH**, namely a considerable slowdown of the $Z \to E$ thermal reversion by almost 23 times for the *o*-fluorinated azo dye (Table 1; Figure S18, Supporting Information). Such a slow relaxation for **azoF** is to be related to the steric and electronic effects exerted by the inductive fluorine atoms that tend to notably stabilize the *Z*-isomer and prevent thermally activated isomerization.[50,51]

Given the stability of **azoF**, nuclear magnetic resonance (NMR) spectroscopy appeared very convenient to assess the photoisomerization efficacy in solution. Despite the simple description of the ^{19}F NMR spectra (Figure S10, Supporting Information), it turns out that ^{1}H NMR spectra provided more reliable results (Figure S11, Supporting Information). Integration of the protons close to the azo moiety gave $E \to Z$ photoconversion yields $\rho_{E\to Z}$ equal to 63 and 65% when irradiating **azoF** at 488 and 550 nm,

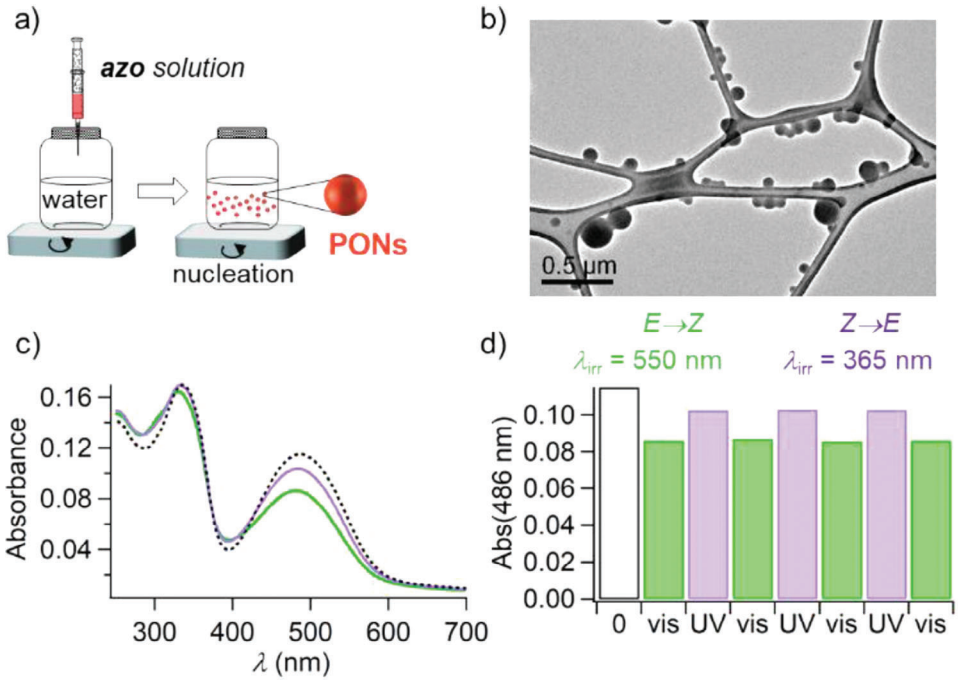

Figure 2. a) Schematic description of flash-nanoprecipitation in the water out of a 1.45×10^{-3} mol L^{-1} **azoF** solution in THF. b) Transmission electron microscopy (TEM) imaging of **azoF** nanoparticles deposited on a holey carbon-coated copper grid. c) Absorption spectra in the water of **azoF** nanoparticles before (dashed line), after 550 nm irradiation (green), and 365 nm irradiation (violet) (10 mW cm^{-2} for 30 s). d) Absorbance at 486 nm upon photoswitching at 550 and 365 nm (10 mW cm^{-2} for 30 s). Absorption spectra of **azoH** and **azoF** in THF solution).

respectively, while keeping the same intensity of 10 mW cm^{-2} (Figure S12, Supporting Information). These results are to be compared to those inferred for **azoH** by resorting to the Fischer's method, and found to be 62 and 81% when irradiating at 488 and 550 nm in the same conditions (Figure S20; Table S1, Supporting Information). Such distinct results corroborate previous experimental data, also emphasizing the use of a green light source to efficiently promote the formation of *Z* isomers in the case of *o*-substituted azo compounds, despite their lower absorbance than that at the absorption maximum.[16] This counterintuitive outcome is to be related to the slightly better-separated energy excited states between the *E* and *Z* *o*-fluorinated isomers, thereby limiting back reversion upon *Z* activation.[48] Besides the distinct probability of photon absorption between the *Z* isomers of **azoF** and **azoH**, the ability of photoisomerizing in the excited state seems also to differ. Indeed, *E*→*Z* photoconversion at 488 nm was found higher for **azoF** compared to **azoH** despite lower absorbing *Z* species. This tends to suggest a higher photoisomerization quantum yield $\Phi_{Z\rightarrow E}$ for **azoF**. However, to go further with this interpretation, thorough wavelength-dependent investigations by ultrafast transient absorption spectroscopy would be highly required, which is beyond the scope of the current studies.

The additional particularity of the present compounds is that irradiation at 365 nm enabled extensive reversion to the initial state leading to a 65 and 63% repopulation of the *E* isomers for **azoH** and **azoF**, respectively. This very unusual result opens up, for the first time to our knowledge, switching in both directions of the photostationary state of strongly push-pull azo compounds.

2.2. Behavior of Nanoparticles with Photoirradiation Cycles

We thus harnessed this new UV irradiation potentiality and the bistability of compound **azoF** to further investigate the geometrical changes undergone by the corresponding nanoparticles in solution. The latter was formed by quick addition into water of a concentrated solution of **azoH** or **azoF** compound in tetrahydrofuran (**Figure 2**a,b). Dynamic light scattering (DLS) and zetametry measurements provided very close hydrodynamic diameters D_Z (147 and 134 nm) for both azo nanoparticles, the smaller value being systematically found for **azoF** (**Table 2**; Figure S21, Supporting Information). This observation agrees with the larger surface potential ζ measured at −27 mV for **azoF** against −21 mV for **azoH**, as a consequence of the enhanced electron density caused by the fluorine substituents located on the electron-withdrawing part. Larger interactions with water are then expected to increase the dye solubility and thereby decrease the size of nanoparticles, issued from a nucleation-aggregation mechanism.[52] Such an assumption is nicely corroborated by the calculations of electrostatic surface potential (Figure S16, Supporting Information). Colloidal stability was found over months for solutions kept at room temperature (19–20 °C), which contrasted with nanoparticles issued from symmetrical *ortho*-fluorinated azo compounds, here dubbed **4F** and **4OMe** (see supporting information), that readily aggregated and decanted in less than 2 h (Figure S17, Supporting Information).

Both **azoH** and **azoF** nanoparticles underwent photoswitching in water upon visible irradiation, albeit to a significantly lesser extent (9 and 20% for **azoH** and **azoF**, respectively, in terms of minimum *E*→*Z* conversion yield ρ^{min}) compared to dyes in

Table 2. Structural, photophysical and photochromic properties of aqueous dispersions of **azoH** and **azoF** nanoparticles.

Cpd	D_Z [nm] (PDI)[a]	ζ [mV][b]	λ_{max} [nm] *E*-isomer (PSS)[c]	τ_1 [min] (f_1 [%])[d]	τ_2 [h] (f_2 [%])[d]	ρ^{min} [%][e]
azoH	147 (0.179)	−21 ± 6	480 (480) 342 (342)	5.3 (17)	2.4 (83)	9
azoF	134 (0.176)	−28 ± 7	484 (481) 333 (331)	75 (34)	30 (66)	20

[a] Determined by DLS; [b] Determined by zetametry; [c] PSS obtained after irradiation at 550 nm (10 mW cm^{-2}); [d] Biexponential mathematical law fitting the recovered absorbance at 481 nm of the *E* species upon back thermal relaxation in the dark at 20 °C, after irradiation at 550 nm until reaching the PSS. τ_i and f_i designate the time constant and averaged amplitude fraction, respectively, with $f_i = a_i / \sum_j a_j$ and $[E] = [E]_0 + a_1\exp(-t/\tau_1) + a_2\exp(-t/\tau_2)$; [e] Minimum conversion yield $\rho^{min} = (A_0 - A_{PSS})/A_0$ where A_0 and A_{PSS} designate the final absorbance after *E* isomer recovery and the absorbance at the photostationary state (550 nm; 10 mW cm^{-2}) respectively, and considering that the *Z* isomers do not absorb.

solution. Interestingly, we found that thermal back relaxation of **azoF** nanoparticles followed the same trend as that reported for dyes in solution (Figures S18 and S19, Supporting Information). Indeed, the kinetics, adequately fitted with a two-exponential law, displayed relaxation time constants τ_i ten times longer for **azoF** with respect to those for **azoH**, while the longer components τ_2 were close to those measured in solution (Table 2). All these results tend to establish that the more distorted **azoF** backbone (dihedral angle of 31° between the azo phenyl rings) prevents extensive quenching upon $\pi-\pi$ aggregation in the solid state.

Owing to the higher thermal stability and larger photoconversion of **azoF** comparatively to **azoH**, we focused our attention on **azoF** for the following studies on photoisomerization cycling. While reverse photoswitching could actually be observed for **azoF** nanoparticles, a slight mismatch between the spectra after the first UV–vis irradiation cycle and right after nanoprecipitation was noticed. This tiny difference, albeit reversible upon UV–vis cycling, was absent for dye solutions (Figure 2c,d). The slight and reversible shift of the isosbestic point between the initial state and the subsequent irradiated states lets us suggest a morphological change that does not impact the chemical integrity of the constituting azo molecules. We thus tried to address this assumption by DLS investigations of the nanoparticle dispersions after 550 or 365 nm irradiation. This however provided unreliable results due to little difference in size apparently. In situ monitoring during irradiation was then performed thanks to the capabilities of the size analyzer to work in a high-rate repetition mode with remote addressing. Contrarily to the common conditions of study, stirring the dispersions was mandatory to reach homogeneous composition and thus avoid progressive replacement of irradiated nanoparticles by non-irradiated ones in the volume addressed by the laser of the DLS setup. Although no size measurements could be inferred in these conditions, photoswitching of the scattered light by nanoparticles was remarkably observed, in direct correlation with the successive visible and UV irradiation steps (**Figure** 3a). Scattering contribution of the excitation source has to be ruled out for two reasons. First, sharp increase in scattering should systematically operate after switching the light on, whatever the wavelength. Here, the scattered light varies in opposite directions (decrease upon green irradiation, and rise for blue irradiation). Second, during light irradiation, the scattered light varies in an exponential manner, evidencing inherent matter transformations.

2.3. In Situ AFM Follow-Up of Nanoparticle Photodeformation

In order to apprehend at the nanoscale the photoinduced morphological evolution of nanoparticles, atomic force microscopy (AFM) imaging, coupled with in situ light irradiation, were undertaken (**Figure** 4a,b). A diluted dispersion of azo nanoparticles was first deposited on a freshly cleaved mica plate. After 1 h, the plate was washed out to remove excess of nanoparticles and recovered with water to let the adsorbed nanoparticles in a wet surrounding. AFM images were recorded on the same scanned areas before irradiation, and right after illumination at 550 or 365 nm. The energy dose was optimized (30 s duration, 1.5 mW cm^{-2} irradiance), so as to avoid irreversible disassembling of the nanoparticles. Before irradiation, AFM imaging, performed on single nanoparticles in the intermittent contact mode to prevent mechanical damages, revealed flattened nanoparticles with a height between 4 and 9 nm. In the following, we looked not only at the height of the nanoparticles, but also evaluated their volume V that provided a more realistic variable parameter to describe the "breathing" of the nanoparticle exposed to light (see supporting information for calculations). Indeed, since azo nanoparticles are photostable in our conditions, any geometry change upon photoisomerization is supposed to induce overall morphological change, especially contraction or expansion. After vis irradiation, we actually measured a 25% decrease in the nanoparticle volume V with respect to the initial volume V_0, while the height sensibly increased for the larger nanoparticle, as a result of matter conservation and lesser compaction effect (Figure 4). After UV irradiation, the nanoparticles notably stretched back and their volume V increased from 8 up to almost 170% for the larger azo nanoparticles.

After a series of UV–vis irradiation cycles, the final nanoparticle volumes with respect to the maximum volume progressively reduced from 80% for the larger nanoparticle after 3 cycles, to 55% for the smaller one after 2 cycles. This evolution emphasized the peculiar behavior of non-covalently bound photochromic nanoparticles that progressively disintegrate upon alternate contraction and stretching, as a "macroscopic" result of the photoinduced motions of their molecular constituents. It is worth noting that a more extensive and faster disintegration occurs with smaller nanoparticles, which could reasonably be ascribed to a larger surface-to-volume ratio and competing interactions with the mica substrate. Indeed, photoisomerization of azo materials has been reported to proceed from the surface to the center where the degrees of freedom are gradually reduced.[53] In the absence of elastic forces as encountered in crosslinked nanoparticles, extensive interactions with the mica surface prevail over intermolecular interactions within the nanoparticles, leading to dispersion of matter. One plausible mechanism to explain such dispersion would rely on the continuous mechanical transformation of the photoinduced change owing to the glassy property of **azoF** material. In such a state, each azo molecule is surrounded by free volume the extension of which is ruled by the external bulky substituents. Since contraction/elongation

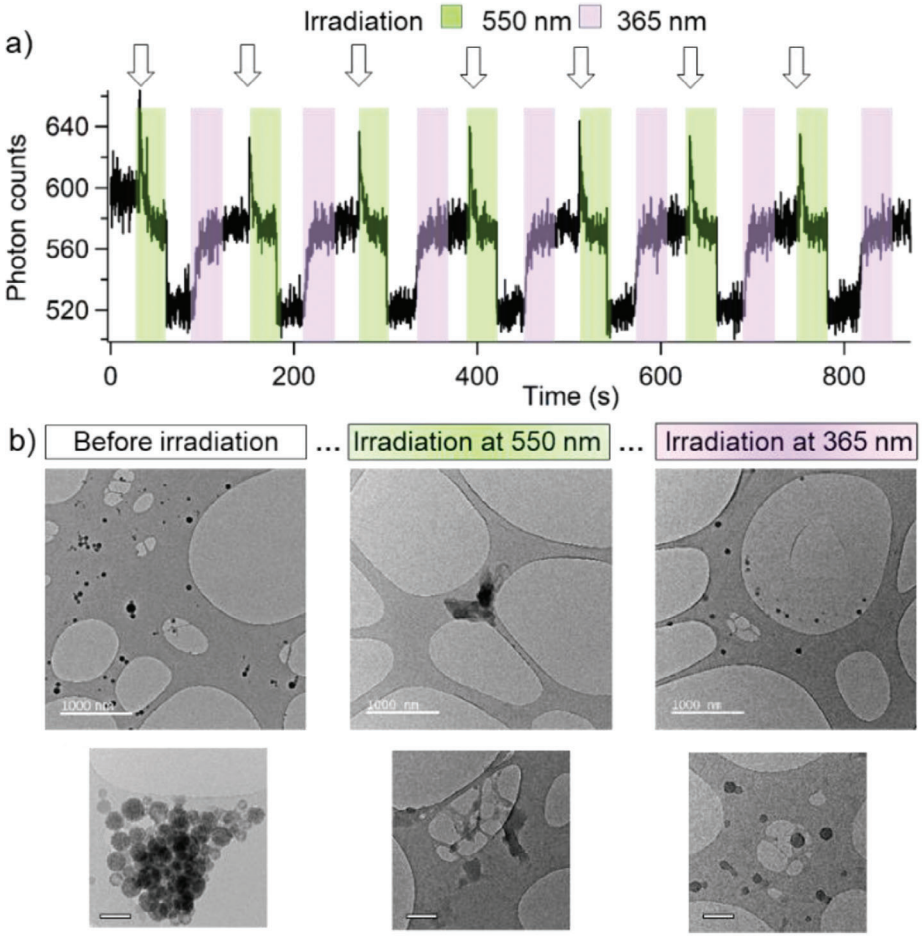

Figure 3. a) Time traces of scattered light (λ = 648 nm) by **azoF** nanoparticle aqueous dispersions using a continuous laser diode from a DLS setup upon alternative irradiation at 550 and 365 nm (10 mW cm^{-2}, 30 s duration for each irradiation condition). White tails display scattered light right after opening the shutter for a 550 nm illumination. b) TEM imaging of aqueous dispersions of **azoF** nanoparticles deposited on holey carbon-coated copper grids before irradiation, after irradiation a 550 nm, and after 550 and 365 nm irradiation (10 mW cm^{-2}, 30 s duration for each irradiation condition). Scale bars: 1000 (top), 200 nm (bottom).

occurs upon photoisomerization, the change in the free volume distribution allows the azo species to extensively physically move in accord with the newly available free volume, unless interactions with surface exert prominent adhesion effects. The effect was particularly striking on an ensemble of nanoparticles whose location appears more resolved in the course of UV–vis light cycles, until vanishing due to extensive flattening (Figure S22, Supporting Information). This behavior recalls similar results with photochromic crystals, amenable to disintegrate and disseminate under irradiation in the presence of a surfactant.[54] In that case, surfactant acts a soap, dissolving one by one the outer molecular layers of the organic crystals while in our case, the surface retains the molecules from the nanoparticle downside and only those on the upper side progressively detach due to looser intermolecular interactions after geometry modifications.

3. Conclusion

In conclusion, resorting to *o*-fluorinated push-pull azo compounds enables the manufacturing of photochromic nanoparticles with long-term colloidal stability in water in the absence of surfactant, and dual *E*-*Z* photoconversion properties. In the absence of covalent bonds between the self-assembled photochromes, progressive disintegration was proved to occur upon alternate irradiation in the visible and UV range. DLS measurements and AFM imaging at the nanoparticle scale, both combined with in situ photoirradiation, and completed with TEM measurements, evidenced differentiated morphology changes upon $E \rightarrow Z$ and $Z \rightarrow E$ photoconversion whether the nanoparticles were dispersed in solution or adsorbed on a surface. The underlying reason is likely to be found in the strong interactions of azo nanoparticles with surfaces, reducing the reversibility of their association/dissociation process. These results shed light on the imperative need to consider the actuating properties of nanomaterials not only in solution, but also in contact with surfaces where adhesion forces can compete with non-covalent intermolecular interactions.[55] This is of utmost important in the field of nanomedicine where azo where close contact of nanoparticles with cell membrane and receptors always precedes any action of drug delivery or ion channel switch.

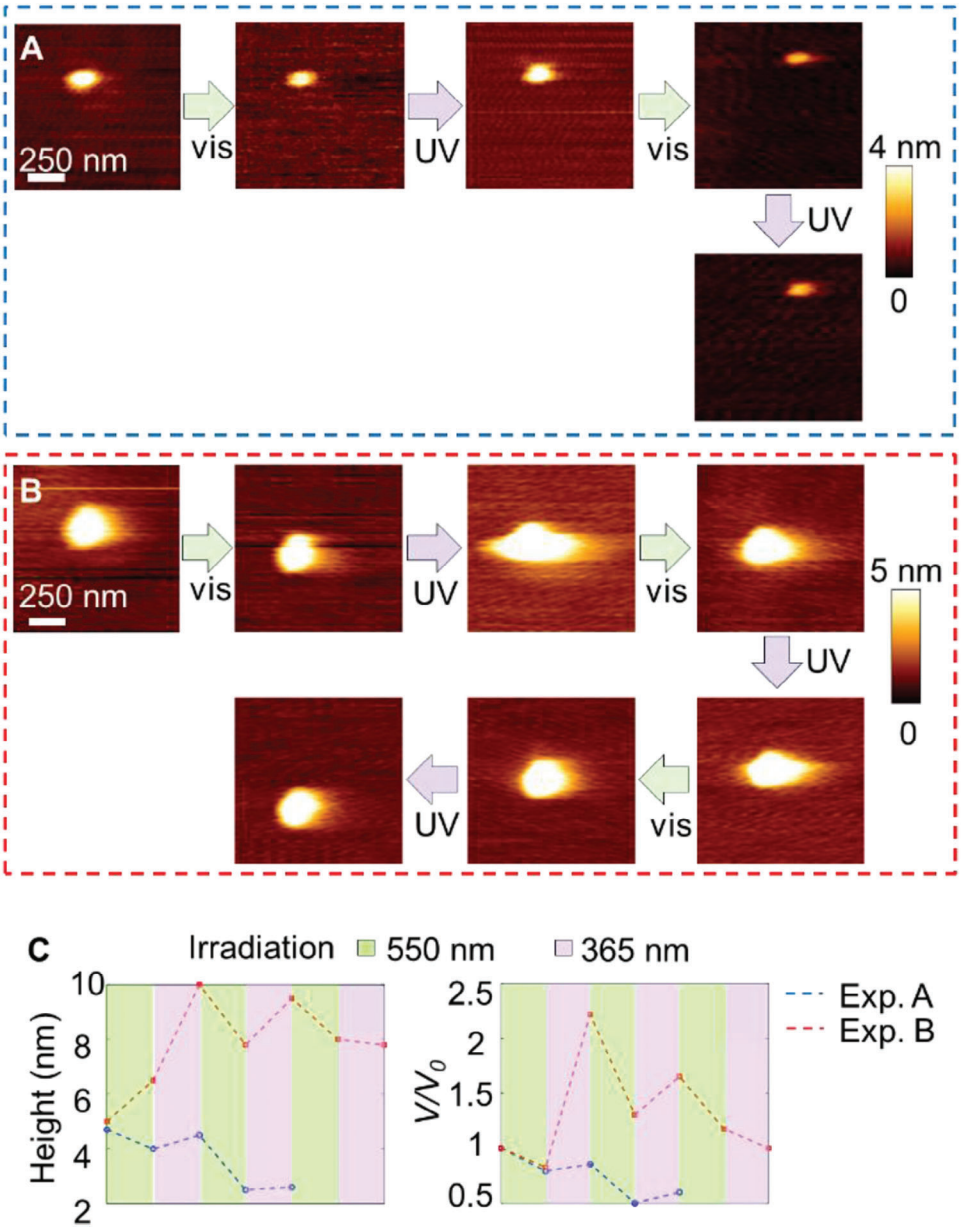

Figure 4. A,B) AFM imaging in water of single **azoF** nanoparticle (A and B) deposited on a freshly cleaved mica sheet upon in situ continuous alternate illumination at 550 and 365 nm (1.5 mW cm^{-2} on the sample for both illumination conditions). C) Evolution of the height and volume ratio with respect to the initial volume V_0 after each sequence of irradiation at 550 and 365 nm.

4. Experimental Section

Materials: All chemical reagents and solvents were purchased from commercial sources and used as received unless otherwise specified. Reactions requiring anhydrous conditions were performed under argon. Purification by column chromatography was conducted on silica gel 60 M (40–63 µ) from Macherey-Nagel and thin layer chromatography reaction monitoring on Merc Silica gel 60 F254 analytical plates with an UV coating (254 or 365 nm).

Structural Characterizations: ^{1}H, ^{13}C NMR, and ^{19}F spectra were recorded on a Bruker Avance 300 MHz spectrometer and chemical shifts were reported in ppm relative to the residual deuterated solvent (7.26 ppm for ^{1}H $CDCl_3$ and 77.16 ppm for ^{13}C $CDCl_3$; 2.50 ppm for ^{1}H $(CD_3)_2SO$ and 39.52 ppm for ^{13}C $(CD_3)_2SO$). High-resolution mass spectra were obtained by ASAP-TOF or ESI-TOF on a Waters Xevo G2-XS QTOF mass spectrometer.

(E)−4-[bis(4′-tert-butylbiphenyl-4-yl)amino)]−4′-(4″-formyl phenyl) −2′,6′-difluoroazobenzene ***azoF***: In a Schlenk tube, the azo derivative **3F** (60 mg, 82 µmol), 4-formylphenylboronic acid (13.6 mg, 91 µmol), and $Pd(PPh_3)_4$ (3 mg, 1 µmol) were dissolved in toluene (1 mL). Ethanol (0.8 mL) and a 2 mol L^{-1} Na_2CO_3 aqueous solution (0.1 mL) were added. The mixture was deoxygenated with argon 4 times and stirred at 80 °C for 15 h, then diluted with toluene, water and brine. The organic layer was separated, dried over anhydrous Na_2SO_4, filtered, and concentrated *in vacuo*. The crude residue was purified by column chromatography (petroleum ether:dichloromethane 1:1) to yield **azoF** as a red solid

(55 mg, 88%). *E*-isomer: ^{1}H (300 MHz, $CDCl_3$): δ 10.1 (s, 1H, H11), 7.97 (d, $J_{10\text{-}9}$ = 9 Hz, 2H, H10), 7.86 (d, $J_{7\text{-}6}$ = 9 Hz, 2H, H7), 7.76 (d, $J_{9\text{-}10}$ = 9 Hz, 2H, H9), 7.55 (d, $J_{3\text{-}2}$ = 9 Hz, 4H, H3), 7.53 (d, $J_{4\text{-}5}$ = 9 Hz, 4H, H4), 7.46 (d, $J_{2\text{-}3}$ = 9 Hz, 4H, H2), 7.30 (d, $J_{8\text{-}F}$ = 9 Hz, 2H, H8), 7.25 (d, $J_{5\text{-}4}$ = 9 Hz, 4H, H5), 7.18 (d, $J_{6\text{-}7}$ = 6 Hz, 2H, H6), 1.36 (s, 18H, H1). ^{13}C NMR ($CDCl_3$, 300 MHz): δ 191.7 (C1), 156.2 (dd, $J_{C\text{-}F}$ = 257 Hz, $J_{C\text{-}F}$ = 6 Hz), 151.6, 150.3, 148.1, 145.5, 144.0, 141.0 (t, $J_{C\text{-}F}$ = 9.8 Hz), 137.5, 137.3, 136.2, 131.4 (t, $J_{C\text{-}F}$ = 9.8 Hz), 130.6, 128.2, 127.6, 126.6, 126.0, 125.9, 124.9, 111.3 (dd, $J_{C\text{-}F}$ = 17.3 Hz, $J_{C\text{-}F}$ = 6.8 Hz) (Car), 34.7, 31.5 (CH_3). ^{19}F NMR (282 MHz, $CDCl_3$): δ −120.45 (s, Far); HRMS (ESI) m/z calcd for $C_{51}H_{46}N_3OF_2$ [$(M + H)^+$] 754.3609, found 754.3613.

(E)−4-[bis(4′-tert-butylbiphenyl-4-yl)amino)]−4′-(4″-formyl phenyl) - azobenzene ***azoH***: In a Schlenk tube, the azo derivative **3H** (70 mg, 0.1 mmol), 4-formylphenylboronic acid (17 mg, 0.11 mmol), and $Pd(PPh_3)_4$ (34.6 mg, 0.03 mmol) were dissolved in toluene (2 mL). Ethanol (0.8 mL) and a 2 mol L^{-1} Na_2CO_3 aqueous solution (23.3 mg, 0.1 mL, 0.22 mmol) were added. The mixture was deoxygenated with argon 4 times and stirred at 80 °C overnight. After cooling down to room temperature, the organic solution was separated, and washed with water and brine. The organic layer was dried over anhydrous Na_2SO_4, filtered, and concentrated *in vacuo*. The crude residue was purified by column chromatography (petroleum ether:dichloromethane 1:1) to yield the final compound **azoH** as a red solid (52 mg, 72%). *E*-isomer: ^{1}H (300 MHz, $CDCl_3$): δ 10.08 (s, 1H, H12), 8.00 (d, $J_{10\text{-}11}$ = 8.7 Hz, 2H, H11), 7.99 (d, $J_{8\text{-}9}$ = 8.1 Hz, 2H, H8), 7.88 (d, $J_{6\text{-}7}$ = 9 Hz, 2H, H7), 7.83 (d, $J_{10\text{-}11}$ = 8.4 Hz, 4H, H10), 7.78 (d, $J_{8\text{-}9}$ = 8.4 Hz, 2H, H9), 7.56 (d, $J_{4\text{-}5}$ = 8.1 Hz, 4H, H4), 7.56 (d, $J_{4\text{-}5}$ = 9 Hz, 4H, H4), 7.55 (d, $J_{2\text{-}3}$ = 8.7 Hz, 4H, H2), 7.47 (d, $J_{2\text{-}3}$ = 8.7 Hz, 4H, H2), 7.27 (d, $J_{4\text{-}5}$ = 8.4 Hz, 2H, H5), 7.23 (d, $J_{6\text{-}7}$ = 9 Hz, 2H, H6), 1.37 (s, 18H). ^{13}C NMR ($CDCl_3$, 300 MHz): δ 192.0, 150.8, 150.3, 147.5, 146.4, 145.9, 141.3, 137.7, 137.0, 135.6, 130.5, 128.2, 128.1, 127.8, 126.6, 125.9, 125.8, 124.6, 123.4, 122.0, 34.7, 31.5. HRMS (ESI) m/z calcd for $C_{51}H_{48}N_3O$ [$(M + H)^+$] 718.3797, found 718.3798.

Thermal Analysis: The glass transition temperature range and proof of the amorphous character of the investigated systems were obtained from classical differential scanning calorimetry (DSC) performed at 30 K.min^{-1}, under a nitrogen flow of 50 mL min^{-1}, over the 20–180 °C temperature window, using a TA Q100 apparatus. The calibration included an empty run to establish the baseline, the cell resistance and capacitance using the Tzero procedure, and a DSC run of indium at 10 K min^{-1} for both temperature and energy. To optimize the sample/sensor contact, the powdered samples in the DSC pan were slowly heated to the liquid state on a Kofler bench. After a first heating-cooling cycle to erase the sample history, two further additional cycles were recorded to inquire about the glass stability of the material.

UV-Absorption and Photochromic Investigations: UV–vis absorption spectra were recorded using a Varian Model Cary 5E spectrophotometer. Molar absorption coefficients were obtained by an average of at least two measurements with less than 10% variation.

Photochromic Investigations: Solutions of azo compounds were prepared at a concentration of ≈2 × 10^{-5} mol L^{-1} in THF solution while the azo nanoparticles dispersions were diluted by five with Millipore water. They were irradiated under vigorous stirring using a H g-Xe light source (Hamamatsu, Lightning Cure LC8), equipped with a quartz fiber and a comprising single-band bandpass filters to irradiate in the visible (550/88 nm BrightLine, Semrock, Optoprim-France retailer), or in the UV (365 nm MaxLamp Mercury line filter, Semrock, Optoprim-France retailer) range. The power was adjusted using a laser power meter (Nova II, Ophir) and a photodiode (PD300/UV/NIR). Back thermal relaxation was recorded from solutions promoted to their photostationary state.

Fabrication of Photochromic Organic Nanoparticles: A stock solution of **azoF** photochromes with a 1.45 mmol L^{-1} concentration was prepared in spectrophotometric grade tetrahydrofuran (THF). A small aliquot (100 µL) was quickly injected in one shot into an 18 mL vial containing Millipore water (2.5 mL) under vigorous stirring by means of a vortex.

Dynamic Light Scattering Measurements: Nanoparticle size measurements in aqueous dispersions were performed via DLS using the VASCO Kin nanoparticle sizer provided by Cordouan Technologies and equipped with a 45 mW diode laser operating at 638 nm. The laser power was manually adjusted for each sample before any measurement to get satisfying results. All measurements were collected on aqueous dispersions at 25 °C in a backscattering mode at a 170° angle, over 2 min with a 5 Hz acquisition frequency, namely every 200 ms. Acquisitions and analyses were done with the Nano Kin software, provided by Cordouan Technologies, Cumulant-based algorithm in intensity was privileged to infer size distributions. A logarithmic scale was adopted for clarity reason, improving visualization of all samples on the same scale, with no impact on the fitted parameters. In situ illumination using a Hamamatsu lamp (Lightning Cure – LC8) equipped with a wheel of narrow bandpass filters (550/88 nm or 365 nm) was performed in a perpendicular direction with respect to that of the scattered light detection. The nanoparticle dispersion was continuously stirred to homogenize the concentration of photo-transformed nanoparticles, while a long-pass optical filter (600 nm) was placed at the front of the detector to minimize light spikes upon illumination. Illumination was performed in a cyclic manned at 550 nm and then 365 nm (irradiance 10 mW cm^{-2}), for a 30 s duration each, while being separated each time by a 30s-lasting dark period (no illumination for 30 s).

Zetametry Measurements: Measurements of surface potential ζ, were carried out by means of a Zetasizer Nano ZS ZEN 3600 (Malvern). The samples were placed in disposable folded capillary cells (DTS1070). Two sets of three measurements were realized for each sample and the zeta potential was calculated from electrophoretic mobility dispersion fitted by the Smoluchowski model.

Transmission Electron Microscopy: Nanoparticle size measurements as dry samples were performed using a MO-Jeol 1230 microscope (80 kV) and a Thermo Fisher Scientific S/TEM Themis Z (300 kV). The samples were prepared from diluted dispersions in water, that were further deposited on holey carbon-coated copper grids (300 mesh), purchased from Agar Scientific.

Atomic Force Microscopy Investigations: All AFM experiments were performed at room temperature (20 °C) using a NanoWizard II atomic force microscope (JPK, Germany) equipped with an inverted optical microscope and x-y closed-loop control system. Cantilevers with silicon tips (App-Nano purchased from Bruker) characterized by a <10 nm ± 2 nm tip radius and 40 N m^{-1} spring constant were used for imaging in intermittent contact mode at a 2 Hz frequency scan. Soft intermittent contact conditions with a low free amplitude (~30 nm) and a set-point ratio close to unity were used to avoid damaging of soft nanoparticles. In situ illumination was performed by mounting right above the AFM chamber through the available optical window the light guide of a Hamamatsu lamp (Lightning Cure – LC8), equipped with a collimating lens and the adapted bandpass filter (550/88 nm or 365 nm). The power was adjusted to provide a ≈1.5 mW cm^{-2} irradiance directly on the sample, after passing through the partly absorbing optical window. In order to calculate the nanoparticle volume, AFM images were flattened by excluding the selected nanoparticle, and the substrate height was used as a height reference. A closed border surrounding the selected nanoparticle was then drawn to extract the height distribution of the nanoparticle. The volume was calculated by numerical integration of the resulting distribution over the nanoparticle area at the substrate level. Interestingly, this method gets rid of any assumption regarding the nanoparticle shape.

Sample Preparation for AFM Measurements: Mica squared plates (1 inch, Oxford) were freshly-cleaved before depositing a small aliquot of nanoparticle aqueous dispersion (100 µL), previously diluted 10 times with Millipore water. After incubation for 1 h, the mica plate was washed, covered with a drop of water, and stuck on a Petri dish, coated with Parafilm to constrain the water droplets on the mica plate.

Synthesis pathways for the precursors of **azoF** and **azoH** compounds and the symmetrical **4-F** and **4-OMe** azo compounds, NMR spectra, thermal analysis, TD-DFT computations, UV–vis spectra, and photochromic properties, description of the Fischer's method, AFM statistical measurements procedure.

Supporting Information

Supporting Information is available from the Wiley Online Library or from the author.

Acknowledgements

CNRS MITI and Nantes University are gratefully acknowledged for their essential financial support through the Interdisciplinary Challenge in Mechanobiology (ENAMEL project), and interdisciplinary call within the NExT i-site excellence initiative (METCIN project), respectively. The French National Research Agency (ANR) and Région Pays de la Loire are strongly acknowledged for their invaluable financial support through the AAPG generic call (grant ANR-21-CE06-0034-01 / AZOTICS project) and the ANR National Trajectory program (grant 27TRAJNAT ANR - n°00153485), respectively. The authors would like to thank very much Dr. Eric Gautron for his patient and careful transmission electron microscopy imaging performed using the IMN's characterization platform PLASSMAT, Nantes, France, as well as Dr. Michael Bailly for his kind and spontaneous help regarding the thermal analysis performed at LTeN, Nantes, France. Dr. Laurence Arzel and Dr. Julie Hemez from the AMAc platform at CEISAM – Nantes University are gratefully acknowledged for their high-quality mass spectrometry analyses. Camille Alvarado and Angelina d'Orlando from the BIBS platform of Nantes-Angers INRA (France) are gratefully acknowledged for their kind advices regarding TEM image acquisition. The Cordouan Technologies Company (Bordeaux, France) was strongly acknowledged for its constant and rich support regarding the analyses of nanoparticle samples.

Conflict of Interest

The authors declare no conflict of interest.

Data Availability Statement

The data that support the findings of this study are available in the supplementary material of this article.

Keywords

AFM addressing, kinetics, nanomechanics, organic nanoparticles, photoswitching

Received: May 14, 2024
Revised: June 30, 2024
Published online: July 12, 2024

[1] T. J. White, *Photomechanical Materials, Composites, and Systems. Wireless Transduction of Light into Work*, John Wiley & Sons, Hoboken, NJ **2017**.
[2] K. Uchida, R. Nishimura, E. Hatano, H. Mayama, S. Yokojima, *Chem.-Eur. J.* **2018**, *24*, 8491.
[3] A. H. Gelebart, D. Liu, D. J. Mulder, K. H. J. Leunissen, J. van Gerven, A. P. H. J. Schenning, D. J. Broer, *Adv. Funct. Mater.* **2018**, *28*, 1705942.
[4] V. Y. Chang, C. Fedele, A. Priimagi, A. Shishido, C. J. Barrett, *Adv. Opt. Mater.* **2019**, *7*, 1900091.
[5] M. Poutanen, O. Ikkala, A. Priimagi, *Macromolecules* **2016**, *49*, 4095.
[6] B. L. Feringa, W. R. Browne, *Molecular Switches*, Wiley-VCH, Weinheim **2011**.
[7] J. Boelke, S. Hecht, *Adv. Opt. Mater.* **2019**, *7*, 1900404.
[8] M. Irie, *Chem. Rev.* **2000**, *100*, 1685.
[9] Y. Kobayashi, J. Abe, *Chem. Soc. Rev.* **2022**, *51*, 2397.
[10] D. Kitagawa, H. Nishi, S. Kobatake, *Angew. Chem., Int. Ed.* **2013**, *52*, 9320.
[11] J. F. R. Van Guyse, Y. Bernhard, A. Podevyn, R. Hoogenboom, *Angew. Chem., Int. Ed.* **2023**, *62*, 202303841.
[12] T. Ikeda, J.-i. Mamiya, Y. Yu, *Angew. Chem., Int. Ed.* **2007**, *46*, 506.
[13] N. P. Pinchin, H. Guo, H. Meteling, Z. Deng, A. Priimagi, H. Shahsavan, *Adv. Mater.* **2024**, *36*, 2303740.
[14] Y. Yu, M. Nakano, T. Ikeda, *Nature* **2003**, *425*, 145.
[15] T. Ube, T. Ikeda, *Angew. Chem., Int. Ed.* **2014**, *53*, 10290.
[16] K. Kumar, C. Knie, D. Bléger, M. A. Peletier, H. Friedrich, S. Hecht, D. J. Broer, M. G. Debije, A. P. H. J. Schenning, *Nat. Commun.* **2016**, *7*, 11975.
[17] C. L. van Oosten, K. D. Harris, C. W. M. Bastiaansen, D. J. Broer, *Eur. Phys. J. E* **2007**, *23*, 329.
[18] P. Naumov, S. Chizhik, M. K. Panda, N. K. Nath, E. Boldyreva, *Chem. Rev.* **2015**, *115*, 12440.
[19] R. O. Al-Kaysi, A. M. Müller, C. J. Bardeen, *J. Am.Chem. Soc.* **2006**, *128*, 15938.
[20] S. Kobatake, S. Takami, H. Muto, T. Ishikawa, M. Irie, *Nature* **2007**, *446*, 778.
[21] K. Imato, N. Kaneda, Y. Ooyama, *Polym. J.* **2024**, *56*, 269.
[22] D. Kwaria, K. McGehee, S. Liu, Y. Kikkawa, S. Ito, Y. Norikane, *ACS Appl. Opt. Mater.* **2023**, *1*, 633.
[23] E. Uchida, R. Azumi, Y. Norikane, *Nat. Commun.* **2015**, *6*, 7310.
[24] S. Saito, S. Nobusue, E. Tsuzaka, C. Yuan, C. Mori, M. Hara, T. Seki, C. Camacho, S. Irle, S. Yamaguchi, *Nat. Commun.* **2016**, *7*, 12094.
[25] H. Nakano, T. Takanashi, T. Kadota, Y. Shirota, *Adv. Mater.* **2002**, *14*, 1157.
[26] Y. Shirota, *J. Mater. Chem.* **2005**, *15*, 75.
[27] S. L. Oscurato, M. Salvatore, P. Maddalena, A. Ambrosio, *Nanophotonics* **2018**, *7*, 1387.
[28] E. Ishow, R. Camacho-Aguilera, J. Guerin, A. Brosseau, K. Nakatani, *Adv. Funct. Mater.* **2009**, *19*, 796.
[29] F. Rodriguez, J. Jelken, N. Delpouve, A. Laurent, B. Garnier, J. L. Duvail, F. Lagugné-Labarthet, E. Ishow, *Adv. Opt. Mater.* **2021**, *9*, 2100525.
[30] T. Fukaminato, S. Ishida, R. Metivier, *NPG Asia Mater.* **2018**, *10*, 859.
[31] E. Campioli, C. Rouxel, M. Campanini, L. Nasi, M. Blanchard-Desce, F. Terenziani, *Small* **2013**, *9*, 1982.
[32] S. Fery-Forgues, *Nanoscale* **2013**, *51*, 8428.
[33] S. Hoang, S. Olivier, S. Cuenot, A. Montillet, J. Bellettre, E. Ishow, *ChemPhysChem* **2020**, *21*, 2502.
[34] N. Fabre, T. Fukaminato, A. Brosseau, M. Sliwa, R. Métivier, *Photochem. Photobiol. Sci.* **2023**, *22*, 1673.
[35] J. Mei, N. L. C. Leung, R. T. K. Kwok, J. W. Y. Lam, B. Z. Tang, *Chem. Rev.* **2015**, *115*, 11718.
[36] J. Su, T. Fukaminato, J. P. Placial, T. Onodera, R. Suzuki, H. Oikawa, A. Brosseau, F. Brisset, R. Pansu, K. Nakatani, R. Metivier, *Angew. Chem., Int. Ed.* **2016**, *55*, 3662.
[37] T. Gallavardin, A. Mulas, L. Norel, S. Rigaut, A. Brosseau, R. Métivier, E. Ishow, *J. Phys. Chem. C* **2021**, *125*, 4665.
[38] J. Boucard, T. Briolay, T. Blondy, M. Boujtita, S. Nedellec, P. Hulin, M. Grégoire, C. Blanquart, E. Ishow, *ACS Appl. Mater. Int.* **2019**, *11*, 32808.
[39] K. Higashiguchi, G. Taira, J.-i. Kitai, T. Hirose, K. Matsuda, *J. Am. Chem. Soc.* **2015**, *137*, 2722.
[40] M. Han, M. Hara, *J. Am. Chem. Soc.* **2005**, *127*, 10951.
[41] S. Lee, S. Oh, J. Lee, Y. Malpani, Y.-S. Jung, B. Kang, J. Y. Lee, K. Ozasa, T. Isoshima, S. Y. Lee, M. Hara, D. Hashizume, J.-M. Kim, *Langmuir* **2013**, *29*, 5869.

[42] E. Fuentes, M. Gerth, J. A. Berrocal, C. Matera, P. Gorostiza, I. K. Voets, S. Pujals, L. Albertazzi, *J. Am. Chem. Soc.* **2020**, *142*, 10069.
[43] D. Manna, T. Udayabhaskararao, H. Zhao, R. Klajn, *Angew. Chem., Int. Ed.* **2015**, *127*, 12571.
[44] D. Horn, J. Rieger, *Angew. Chem., Int. Ed.* **2001**, *40*, 4330.
[45] Z. Chu, Y. Han, T. Bian, S. De, P. Král, R. Klajn, *J. Am. Chem. Soc.* **2019**, *141*, 1949.
[46] D. Bléger, S. Hecht, *Angew. Chem., Int. Ed.* **2015**, *54*, 11338.
[47] F. A. Jerca, V. V. Jerca, R. Hoogenboom, *Nat. Rev. Chem.* **2022**, *6*, 51.
[48] E. Ishow, B. Lebon, Y. N. He, X. G. Wang, L. Bouteiller, L. Galmiche, K. Nakatani, *Chem. Mater.* **2006**, *18*, 1261.
[49] K. E. Snell, J.-Y. Mevellec, B. Humbert, F. Lagugné-Labarthet, E. Ishow, *ACS Appl. Mater. Int.* **2015**, *7*, 1932.
[50] Z. Ahmed, A. Siiskonen, M. Virkki, A. Priimagi, *Chem. Commun.* **2017**, *53*, 12520.
[51] C. Knie, M. Utecht, F. Zhao, H. Kulla, S. Kovalenko, A. M. Brouwer, P. Saalfrank, S. Hecht, D. Bléger, *Chem.-Eur. J.* **2014**, *20*, 16492.
[52] M. Breton, G. Prevel, J. F. Audibert, R. Pansu, P. Tauc, B. Le Pioufle, O. Francais, J. Fresnais, J. F. Berret, E. Ishow, *Phys. Chem. Chem. Phys.* **2011**, *13*, 13268.
[53] C. J. Barrett, A. L. Natansohn, P. L. Rochon, *J. Phys. Chem.* **1996**, *100*, 8836.
[54] F. Tong, S. Chen, Z. Li, M. Liu, R. O. Al-Kaysi, U. Mohideen, Y. Yin, C. J. Bardeen, *Angew. Chem., Int. Ed.* **2019**, *58*, 15429.
[55] D. K. Hohl, C. Weder, *Adv. Opt. Mater.* **2019**, *7*, 1900230.